Different Interaction between the Agonist JN403 and the Competitive Antagonist Methyllycaconitine with the Human α7 Nicotinic Acetylcholine Receptor

4 AUTHORS, INCLUDING:

Dominik Feuerbach
Novartis Institutes for BioMedical Research
63 PUBLICATIONS **1,167** CITATIONS

Dong-Qing Wei
Shanghai Jiao Tong University
224 PUBLICATIONS **4,651** CITATIONS

Different Interaction between the Agonist JN403 and the Competitive Antagonist Methyllycaconitine with the Human α7 Nicotinic Acetylcholine Receptor[†]

Hugo R. Arias,*[,‡,⊥] Ruo-Xu Gu,[§,⊥] Dominik Feuerbach,[∥] and Dong-Qing Wei[§]

[‡]*Department of Pharmaceutical Sciences, College of Pharmacy, Midwestern University, Glendale, Arizona 85308,* [§]*College of Life Science and Biotechnology, Shanghai Jiaotong University, Shanghai, China, and* [∥]*Neuroscience Research, Novartis Institutes for Biomedical Research, Basel, Switzerland* [⊥]*These authors contributed equally to this work.*

ABSTRACT: The interaction of the agonist JN403 with the human (h) α7 nicotinic acetylcholine receptor (AChR) was compared to that for the competitive antagonist methyllycaconitine (MLA). The receptor selectivity of JN403 was studied on the hα7, hα3β4, and hα4β2 AChRs. The results established that the cationic center and the hydrophobic group found in JN430 and MLA are important for the interaction with the AChRs. MLA preincubation inhibits JN403-induced Ca^{2+} influx in GH3-hα7 cells with a potency 160-fold higher than that when MLA is co-injected with JN403. The most probable explanation, based on our dynamics results, is that MLA (more specifically the 3-methyl-2,5-dioxopyrrole ring and the B−D rings) stabilizes the resting conformational state. The order of receptor specificity for JN403 is as follows: hα7 > hα3β4 (∼40-fold) > hα4β2 (∼500-fold). This specificity is based on a larger number of hydrogen bonds between the carbamate group (another pharmacophore) of JN403 and the hα7 sites, the electrostatic repulsion between the positively charged residues around the hα3β4 sites and the cationic center of JN403, fewer hydrogen bonds for the interaction of JN403 with the hα3β4 AChR, and an unfavorable van der Waals interaction between JN403 and the α4−β2 interface. The higher receptor specificity for JN403 could be important for the treatment of α7-related disorders, including dementias, pain-related ailments, depression, anxiety, and wound healing.

The nicotinic acetylcholine receptor (AChR)[1] family is genetically and structurally related to the Cys-loop ligand-gated ion channel superfamily that also includes the glycine, type 3 serotonin, and type A and C GABA receptors (reviewed in refs *1−3*). AChRs are pentameric structures that can be formed by just one subunit subtype, the so-called homomeric receptors (e.g., α7−α9), or by more than one subunit subtype, the so-called heteromeric receptors (e.g., α4β2, α3β4, etc.). α7 AChRs can be pharmacologically and functionally distinguished from other AChR subtypes because they have a high affinity for the competitive antagonist α-bungarotoxin (α-BTx), a low affinity for the agonist (−)-nicotine, and high Ca^{2+}/Na^+ permeability ratios, can be fully activated by choline, and desensitize very rapidly, whereas AChRs such as the α4β2 subtype have a high affinity for (−)-nicotine, a low affinity for α-BTx, and lower Ca^{2+}/Na^+ permeability ratios, cannot be activated by choline, and desensitize more slowly. α7 AChRs are one of the most prominent receptors in the brain, and they are found in particular areas such as cortex, substantia nigra, ventral tegmental area, amygdala, hypothalamus, hippocampus, cerebellum, and olfactory bulb (reviewed in ref *2*). In addition to neuronal locations, α7 AChRs are expressed in several non-neuronal cells (reviewed in ref *4*). In this regard, several physiological functions have been inferred, including modulation of neurotransmitter release, drug reward, and angiogenesis (reviewed in refs *2−4*). From the pathophysiological point of view, α7 AChRs are implicated in diseases such as Alzheimer's disease, schizophrenia, drug addiction, neuronal and peripheral inflammation, and cancer (reviewed in refs *2−6*). In this regard, an improved understanding of the interaction of agonists and antagonists with AChRs, and in particular with α7 AChRs, is crucial to the development of more specific and, consequently, safer ligands for different therapeutic purposes.

There are several natural compounds that present a relatively high specificity for the α7 AChR, including antagonists such as the snake toxin α-BTx (reviewed in ref *7*), the snail toxin α-conotoxin ImI (*8*), and the alkaloid methyllycaconitine (MLA) (*9*). However, several pharmacokinetic and metabolic properties prevent them from being therapeutically useful. In this regard, various small molecules have been synthesized and are in preclinical or clinical stages for the treatment of some of the α7 AChR-related diseases

*To whom correspondence should be addressed: Department of Pharmaceutical Sciences, College of Pharmacy, Midwestern University, 19555 N. 59th Ave., Glendale, AZ 85308. Telephone: (623) 572-3589. Fax: (623) 572-3550. E-mail: harias@midwestern.edu.

[1]Abbreviations: AChR, nicotinic acetylcholine receptor; [³H]MLA, [³H]methyllycaconitine; α-BTx, α-bungarotoxin; JN403, (*S*)-(1-azabicyclo[2.2.2]oct-3-yl)carbamic acid (*S*)-1-(2-fluorophenyl)ethyl ester; CCh, carbamylcholine; RT, room temperature; BS buffer, binding saline buffer [50 mM Tris-HCl, 120 mM NaCl, 5 mM KCl, 2 mM $CaCl_2$, and 1 mM $MgCl_2$ (pH 7.4)]; K_i, inhibition constant; K_d, dissociation constant; IC_{50}, ligand concentration that produces 50% inhibition (of binding or of agonist activation); n_H, Hill coefficient; EC_{50}, agonist concentration that produces 50% AChR activation; DMEM, Dulbecco's modified Eagle's medium; FBS, fetal bovine serum; FLIPR, fluorescent imaging plate reader.

mentioned above (reviewed in ref *3*). One of these compounds, JN403 [(*S*)-(1-azabicyclo[2.2.2]oct-3-yl)carbamic acid (*S*)-1-(2-fluorophenyl)ethyl ester], is a partial but potent α7 AChR agonist (*10*) that has beneficial properties, improving cognition and sensory gating deficits and decreasing pain, epileptic seizures, and anxiety (*11*). The pharmacokinetic studies of JN403 indicate that this compound is stable in other complex systems, i.e., in animals and during the extraction process. Additional compounds include benzylidene-anabaseine analogues (*12*, *13*) (reviewed in ref *14*) and novel γ-lactam derivatives (*15*).

We want to determine the interaction of the specific agonist JN403 with the hα7 AChR and compare it with that for the potent competitive antagonist MLA. To determine the structural basis of receptor specificity, we performed additional structural and functional studies with the agonist JN403 at the hα3β4 and hα4β2 AChRs. In this regard, we applied structural and functional approaches, including radioligand binding assays using [³H]MLA on SH-SY5Y-hα7 cell membranes, [³H]epibatidine on HEK293-hα3β4 cell membranes, and [³H]cytisine on HEK293-hα4β2 cell membranes, as well as Ca^{2+} influx-induced fluorescence detection in GH3-hα7 cells, and molecular docking and dynamics studies. The final purpose of this study is to characterize the pharmacophore for the hα7 AChR to develop more specific ligands for potential clinical uses. In this regard, JN403 is a specific agonist for the hα7 AChR that could be used for the treatment of Alzheimer's disease, schizophrenia, pain-related diseases, and depression and anxiety (*11*), as well as wound healing (H. R. Arias et al., manuscript in preparation).

EXPERIMENTAL PROCEDURES

Materials. [³H]Epibatidine (45.1 Ci/mmol) and [³H]cytisine (35.6 Ci/mmol) were obtained from PerkinElmer Life Sciences Products, Inc. (Boston, MA). [³H]Methyllycaconitine (100 Ci/mmol) was purchased from American Radiolabeled Chemicals Inc. (St. Louis, MO). The radioligands were stored in ethanol at −20 °C. Methyllycaconitine citrate, carbamylcholine chloride (CCh), polyethylenimine, leupeptin, bacitracin, pepstatin A, aprotinin, benzamidine, phenylmethanesulfonyl fluoride, sucrose, and sodium azide were purchased from Sigma Chemical Co. (St. Louis, MO). (±)-Epibatidine hydrochloride, Geneticin, and hygromycine B were obtained from Tocris Bioscience (Ellisville, MO). Fetal bovine serum (FBS), trypsin, and EDTA were purchased form Gibco BRL (Paisley, U.K.). Ham's F-12 Nutrient Mixture was obtained from Invitrogen (Paisley, U.K.). JN403 was synthesized as previously described (*10*). Salts were of analytical grade.

Cell Culture Procedures. The source and cell culture procedures for the HEK293-hα3β4 and HEK293-hα4β2 cells (*16*), as well as for the GH3-hα7 (*17*) and SH-SY5Y-hα7 (*18*) cells, were the same as those previously described. HEK293-hα3β4 and HEK293-hα4β2 cells were cultured in a 1:1 mixture of Dulbecco's modified Eagle's medium containing 3.7 g/L NaHCO₃ and 1.0 g/L sucrose, supplemented with stable glutamine (L-alanyl-L-glutamine, 524 mg/L), and Ham's F-12 Nutrient Mixture containing 1.176 g/L NaHCO₃ and supplemented with 10% (v/v) FBS, Geneticin (0.2 mg/mL), and hygromycin B (0.2 mg/mL). GH3-hα7 cells were cultured in Ham's F-12 Nutrient Mixture with 1.176 g/L NaHCO₃ and stable glutamine, supplemented with 10% (v/v) FBS and 50 μg/mL Geneticin. SH-SY5Y-hα7 cells were cultured in Dulbecco's modified Eagle's medium supplemented with 10% (v/v) FBS and 100 μg/mL Geneticin. All cells

were cultured at 37 °C in 5% CO_2 at 95% relative humidity and passaged every 3 days by being detached from the cell culture flask by being washed with phosphate-buffered saline and a brief incubation (∼3 min) with trypsin (0.5 mg/mL) and EDTA (0.2 mg/mL).

Preparation of Native Membranes from Cells Expressing Different AChR Subtypes. To prepare cell membranes in large quantities, we cultured HEK293-hα3β4, HEK293-hα4β2, and SH-SY5Y-hα7 cells separately in suspension using non-treated Petri dishes (150 mm × 15 mm) as previously described (*19*, *20*). After the cells had been cultured for ∼2 weeks, cells were harvested by being gently scraped and centrifuged at 1000 rpm for 5 min at 4 °C using a Sorvall Super T21 centrifuge. Cells were resuspended in binding saline (BS) buffer [50 mM Tris-HCl, 120 mM NaCl, 5 mM KCl, 2 mM $CaCl_2$, and 1 mM $MgCl_2$ (pH 7.4)] containing 0.025% (w/v) sodium azide and a cocktail of protease inhibitors, including leupeptin, bacitracin, pepstatin A, aprotinin, benzamidine, and phenylmethanesulfonyl fluoride. The suspension was maintained on ice, homogenized using a Polytron PT3000 (Brinkmann Instruments Inc., Westbury, NY), and then centrifuged at 10000 rpm for 30 min at 4 °C. The pellet was finally resuspended in BS buffer containing 20% (w/v) sucrose using the Polytron and briefly (6 × 15 s) sonicated (Branson Ultrasonics Co., Danbury, CT) to ensure maximum homogenization. Cell membranes containing hα7, hα3β4, and hα2β2 AChRs were frozen at −80 °C until they were required. The total amount of protein was determined using the bicinchoninic acid protein assay (Thermo Fisher Scientific, Rockford, IL).

Ca^{2+} *Influx Measurements in GH3-hα7 Cells*. Ca^{2+} influx was determined as previously described (*17*). Briefly, 5 × 10⁴ GH3-hα7 cells per well were seeded 72 h prior to the experiment on black 96-well plates (Costar) and incubated at 37 °C in a humidified atmosphere (5% CO_2/95% air); 16−24 h before the experiment, the medium was changed to 1% bovine serum albumin (BSA) in HEPES-buffered salt solution (HBSS) [130 mM NaCl, 5.4 mM KCl, 2 mM $CaCl_2$, 0.8 mM $MgSO_4$, 0.9 mM NaH_2PO_4, 25 mM glucose, and 20 mM HEPES (pH 7.4)]. On the day of the experiment, we removed the medium by flicking the plates and replaced it with 100 μL of an HBSS/1% BSA mixture containing 2 μM Fluo-4 (Molecular Probes, Eugene, OR) in the presence of 2.5 mM probenecid (Sigma, Buchs, Switzerland). The cells were then incubated at 37 °C in a humidified atmosphere (5% CO_2/95% air) for 1 h. Plates were flicked to remove excess of Fluo-4, washed twice with an HBSS/1% BSA mixture, and finally refilled with 100 μL of HBSS containing different concentrations of MLA and incubated for 5 min at RT. Plates were then placed in the cell plate stage of the fluorescent imaging plate reader (FLIPR) (Molecular Devices, Sunnyvale, CA). JN403 was added to the cells using the FLIPR 96-tip pipettor while fluorescence was being recorded for a total length of 3 min. In parallel experiments, 0.1 μM JN403 was co-injected with different concentrations of MLA. A baseline consisting of five measurements of 0.4 s each was recorded. The laser excitation and emission wavelengths were 488 and 510 nm, respectively, at 1 W, with a CCD camera opening of 0.4 s.

Radioligand Competition Binding Experiments. We studied the influence of MLA and JN403 on the binding of specific radioligands for the hα7 ([³H]MLA), hα3β4 ([³H]epibatidine), and hα4β2 ([³H]cytisine) AChRs. In this regard, AChR membranes (1.5 mg/mL) were suspended in BS buffer with 4 nM [³H]MLA (hα7), 8 nM [³H]epibatidine (hα3β4), or 9 nM

[³H]cytisine (hα4β2) and preincubated for 30 min at RT. The level of nonspecific binding was determined in the presence of 10 μM MLA ([³H]MLA), 0.5 μM (±)-epibatidine ([³H]epibatidine), or 1 mM CCh ([³H]cytisine). The total volume was divided into aliquots, and increasing concentrations of the ligand under study were added to each tube and incubated for 2 h at RT. AChR-bound radioligand was then separated from free radioligand by a filtration assay using a 48-sample harvester system with GF/B Whatman filters (Brandel Inc., Gaithersburg, MD), previously soaked with 0.5% polyethylenimine for 30 min. The membrane-containing filters were transferred to scintillation vials with 3 mL of Bio-Safe II (Research Product International Corp., Mount Prospect, IL), and the radioactivity was determined using a Beckman LS6500 scintillation counter (Beckman Coulter, Inc., Fullerton, CA).

The concentration−response data were curve-fitted by non-linear least-squares analysis using Prism (GraphPad Software, San Diego, CA). The corresponding IC_{50} values were calculated using the following equation:

$$\theta = 1/[1 + ([L]/IC_{50})^{n_H}] \qquad (1)$$

where θ is the fractional amount of the radioligand bound in the presence of the inhibitor at a concentration [L] compared to the amount of the radioligand bound in the absence of inhibitor (total binding), IC_{50} is the inhibitor concentration at which $\theta = 0.5$ (50% bound), and n_H is the Hill coefficient. The observed IC_{50} values for JN403 and MLA from the competition experiments described above were transformed into inhibition constant (K_i) values using the Cheng−Prusoff relationship (*21*):

$$K_i = IC_{50}/(1 + [[^3H]ligand]/K_d^{ligand}) \qquad (2)$$

where [[³H]ligand] is the initial concentration of [³H]MLA, [³H]epibatidine, or [³H]cytisine and K_d^{ligand} is the dissociation constant for [³H]MLA (1.86 nM) (*9*), [³H]epibatidine (0.089 nM) (*17*), or [³H]cytisine (0.3 nM) (*22*) for the respective AChR subtype. The calculated K_i and n_H values are summarized in Table 2.

Homology Models of the hα3β4, hα4β2, and hα7 AChRs. The homology model of the hα7 AChR was constructed as described previously (*13*, *23*) and then used in docking and molecular dynamics simulation studies. The sequence alignment and homology modeling of the hα3β4 AChR were created using an in-house program SAMM (Shanghai Molecule Modeling) based on the crystal structure of the acetylcholine binding protein [AChBP; Protein Data Bank (PDB) entry 1i9b] (*24*). In this regard, the extracellular domains of the α3 (i.e., residues 33−240) and β4 (i.e., residues 26−233) subunits were used. The procedures of homology modeling are described as follows. (1) The three-dimensional (3D) structure of the first α3 subunit was generated by the segment matching approach based on chain A of AChBP with the other four chains present as the environment. (2) The 3D structure of the first β4 subunit was generated on the basis of chain B of AChBP with the homology model of the α3 subunit and the crystal structure of the other three chains of AChBP as the environment. Finally, (3) the homology model of the second α3 subunit and the second and third β4 subunits was constructed using the same method. In this manner, 10 structures were constructed, and the calculated average of these structures was used in docking and molecular dynamics simulations. To construct the homology model of the hα4β2 AChR, the same method described for the hα3β4 AChR was used, where the extracellular

domains of the α4 (i.e., residues 36−247) and β2 (i.e., residues 28−234) subunits were used instead.

Molecular Docking. To compare the interaction between agonists and competitive antagonists on the hα7 AChR, we docked the specific agonist JN403 and the potent competitive antagonist MLA to the binding domain of the hα7 AChR. To determine the structural basis of receptor specificity, we also docked the agonist JN403 to the hα3β4 and hα4β2 AChRs.

Ligands were first placed in the vicinity of the binding cavity proposed by Unwin (*25*), and subsequently, docking simulations were conducted using AutoDock version 3.0.5 (*26*). The genetic algorithm was used to perform 100 independent runs at each binding site on a 40 Å cubic grid centered on the mass center of the ligand with a grid spacing of 0.375 Å.

Molecular Dynamics Simulations. Molecular dynamics simulations of the JN403−hα7 AChR, MLA−hα7 AChR, JN403−hα3β4 AChR, and JN403−hα4β2 AChR complexes were performed in a dodecahedron box with GROMACS96 43a1 force field parameters using GROMACS version 3.1.1 (*27*). The single-point-charge (SPC) water model was used to solvate the complex, and Na⁺ ions were added as counterions to neutralize the system via random replacement of the water molecules. Each system contains a total of ∼85000 atoms. Molecular dynamics simulations were conducted with an integration time step of 2 fs with a constant number of atoms under a constant volume and a constant temperature (i.e., NPT ensemble), using Berendsen's algorithm to keep the temperature at 310 K and the pressure at 1 atm. Periodic boundary conditions were employed in all three dimensions, and the LINCS algorithm (*28*) was used to constrain all bonds in the system. A cutoff of 1.4 Å was used to account for the van der Waals interactions. In addition, the particle mesh Ewald (PME) method was used to account for the long-range electrostatic interactions. The detailed simulation procedure is as follows. First, 3000 steps of energy minimization were performed to relax the system before dynamics simulations. Second, a brief (500 ps) simulation was conducted with the backbone of the protein constrained to fully solvate the system. Finally, a 10 ns simulation was performed without any constraint.

Analysis Methods for Molecular Dynamics Simulations. The five α7 subunits are called subunits a, b, c, d, and e, and their subunit interfaces are named I_{ab}, I_{bc}, I_{cd}, I_{de}, and I_{ea}, respectively. For example, I_{ab} is the interface between primary subunit a and complementary subunit b. A similar nomenclature is used for the hα3β4 and hα4β2 AChRs. For instance, in the hα3β4 (or hα4β2) AChR, the two α3 (or α4) subunits are named b and d, and I_{bc} and I_{de} are the respective α−β interfaces that can accommodate the agonist molecules. All molecules, residues, and proteins in the pictures are drawn by using Visual Molecular Dynamics (VMD).

The default hydrogen bond definition of GROMACS was used in our study: a hydrogen bond is considered to be formed if the distance between the heavy atoms of the hydrogen bond donor and acceptor is less than 3.5 Å and the hydrogen atom−donor−acceptor angle is less than 30°.

The distance between the mass center of Trp149 and the mass center of Tyr188 and the distance between the mass center of Trp149 and the mass center of Tyr195 from the hα7 AChR were calculated by the g_dist command in GROMACS.

To determine the motion of loop C (see Supporting Information 1 for loop nomenclature), we calculated both the distance and the Z coordinate of the α-carbon (Cα) of Cys190, which is

located in loop C, from the central axis of the pentamer as a function of time. The line expressed by the following equation is considered as the central axis of the pentamer:

$$x = \sum_{i=1}^{N} x_i/N, \; y = \sum_{i=1}^{N} y_i/N \tag{3}$$

where N is the number of $C\alpha$ atoms in the pentamer and x_i and y_i refer to the x and y coordinates of the ith $C\alpha$ atom, respectively. Then, the distance from atom i to the central axis, r_i, is calculated as

$$r_i = \sqrt{(x_i' - x)^2 + (y_i' - y)^2} \tag{4}$$

where x_i' and y_i' are the x and y coordinates of atom i, respectively.

The radius of gyration of the subunit, R_g, describing whether the subunit moves toward or away from the pentamer central axis, is defined as

$$R_g = \left(\sum m_i r_i^2 / \sum m_i\right)^{1/2} \tag{5}$$

where m_i is the mass of the atom and r_i is the distance from the atom to the central axis calculated by eq 4. Only $C\alpha$ is used in the calculation.

The axis of the JN403 molecule is defined as the line determined by the two carbon atoms at the two ends of the flexible chain that contains an ester bond from the JN403 molecule.

Calculations of the Binding Free Energy. Well-known methods for binding free energy calculations, including MM-PBSA (molecular mechanics Poisson–Boltzmann/surface area) and its variant MM-GBSA (molecular mechanics generalized Born/surface area) (*29*), were applied to study the interaction of JN403 at the $\alpha7$–$\alpha7$, $\alpha3$–$\beta4$, and $\alpha4$–$\beta2$ interfaces. The change in free energy (ΔG) during formation of the ligand–receptor complex was defined by the following equation:

$$\Delta G = G_{complex} - G_{receptor} - G_{ligand} \tag{6}$$

where $G_{complex}$, $G_{receptor}$, and G_{ligand} refer to the free energy of the complex, receptor, and ligand, respectively. According to the MM-PBSA/GBSA methods, the free energy of a molecule can be calculated as

$$G_{molecule} = \langle E_{MM}\rangle + \langle G_{Solv}\rangle - \langle TS\rangle \tag{7}$$

where $\langle E_{MM}\rangle$, $\langle G_{Solv}\rangle$, and $\langle TS\rangle$ denote the molecular mechanics energy, solvation energy, and entropy contributions, respectively. The angle brackets denote the average of a series of conformations. For the calculation of $\langle E_{MM}\rangle$, it is decomposed in three parts:

$$\langle E_{MM}\rangle = \langle E_{int}\rangle + \langle E_{ele}\rangle + \langle E_{vdw}\rangle \tag{8}$$

where $\langle E_{int}\rangle$ is the internal energy, including the bond stretching energy, the angle bending energy, and the dihedral torsion energy; $\langle E_{ele}\rangle$ is the electrostatic interaction energy; and $\langle E_{vdw}\rangle$ is the van der Waals interaction energy. In turn, the solvation energy $\langle G_{Solv}\rangle$ can by calculated by

$$\langle G_{Solv}\rangle = \langle G_{nonpolar}\rangle + \langle G_{polar}\rangle \tag{9}$$

where $\langle G_{nonpolar}\rangle$ and $\langle G_{polar}\rangle$ correspond to the nonpolar and polar solvation energies, respectively. $\langle G_{nonpolar}\rangle$ is estimated by scaling the molecular surface by a specific constant,

using the following equation:

$$G_{nonpolar} = (\text{surften} \times \text{SASA}) + \text{surfoff} \tag{10}$$

where surften and surfoff were set to 0.0072 and 0.00, respectively, as previously used (*30*), and SASA denotes the solvent accessible surface area. In the MM-PBSA calculations, a solvent probe with a radius of 1.4 Å is used to detect the SASA, whereas in MM-GBSA, the LCPO (linear combinations of pairwise overlaps) method is used to estimate the SASA. In the MM-PBSA method, $\langle G_{polar}\rangle$ is calculated by solving the Poisson–Boltzmann equation (PBE), whereas in the MM-GBSA method, it is estimated by the generalized Born equation. The standard parameters in the AMBER package are used in the calculation of $\langle G_{polar}\rangle$. More specifically, in the MM-PBSA calculations, the internal and external dielectric constants were set to 1.0 and 80.0, respectively, and a salt concentration of 0.0 was used. After the grids had been centered on the molecule with a grid spacing of 0.5 Å, 1000 iteration steps were performed to solve the linear PBE, while in the MM-GBSA calculations, the same dielectric constants and salt concentration were used.

The E_{MM} terms ($\langle E_{int}\rangle$, $\langle E_{ele}\rangle$, and $\langle E_{vdw}\rangle$) and G_{Solv} terms ($\langle G_{nonpolar}\rangle$ and $\langle G_{polar}\rangle$) were calculated by the *sander* and *pbsa* modules of the AMBER package, respectively. Since the calculation of $\langle TS\rangle$, which can be estimated from normal model analysis, is expensive in terms of computational time and often introduces additional uncertainty into the calculated free energy, it was not included in our calculation.

Since each energy term is an average, it is necessary to generate a collection of conformations from the complexes, receptors, and ligands to calculate their binding free energy by the MM-PBSA/GBSA methods. These conformations can be obtained by using the single-trajectory and three-trajectory methods. The three-trajectory method is based on the performance of independent molecular dynamics simulations on the complex, receptor, and ligand, and the needed conformations can be extracted, consequently, from three separated trajectories. In the single-trajectory method, only one dynamics simulation is conducted and the conformations of the complex, receptor, and ligand are extracted from the same trajectory. The single-trajectory method was employed in our calculations by performance of 3 ns molecular dynamics simulations on the interaction between JN403 and the $\alpha7$–$\alpha7$, $\alpha3$–$\beta4$, and $\alpha4$–$\beta2$ interfaces with AMBER8 (*31*). Since the $\alpha7$–$\alpha7$, $\alpha3$–$\beta4$, and $\alpha4$–$\beta2$ interfaces were used in this dynamics sampling, the $C\alpha$ atoms were restrained by a force constant of 2 kcal mol^{-1} Å^{-2} to prevent conformational deformations of the complexes (see Supporting Information 2 for the details on the simulation protocol). In addition, 50 snapshots of the complexes, receptors, and ligands, which were used to calculate the free energies of interaction, were extracted from the last 2 ns of the trajectory at an interval of 40 ps.

The computational Ala-scanning method (*32*) was used to explore the mutational effects on several residues proved by dynamics simulations to be pivotal in ligand–receptor binding (see Supporting Information 6). Among the most important residues, we studied Trp55, Phe104, Val108, Leu119, Gln57, and Gln117 from the complementary component of the $\alpha7$–$\alpha7$ interface; Tyr93, Trp149, Tyr188, and Tyr195 from the primary component of the $\alpha7$–$\alpha7$ interface; Tyr90, Trp146, Tyr187, and Tyr194 from subunit $\alpha3$; and Trp55, Ile109, Leu117, Leu119, Lys32, Lys57, Glu59, and Arg111 from subunit $\beta4$. These residues were mutated to Ala, and the binding free energies were calculated by the methods explained above.

RESULTS

Ligand Activity Assessed by Ca^{2+} Influx in GH3-hα7 Cells.
The potency of JN403 in activating the hα7 AChR was compared
to that for ($\pm$)-epibatidine via assessment of the fluorescence
change in GH3-hα7 cells after agonist stimulation (Figure 1).
JN403 stimulated the hα7 AChR with practically the same efficacy
as ($\pm$)-epibatidine but with a 2-fold lower potency [EC$_{50}$ = 103 $\pm$
8 nM (Table 1)] compared to that for ($\pm$)-epibatidine (EC$_{50}$ = 52 $\pm$
4 nM). The fact that the n_H value is greater than 2 (Table 1)
indicates that the stimulatory process mediated by JN403 is
produced in a cooperative manner. This in turn suggests that
JN403 interacts with more than one binding site. This result is not
surprising because the α7 AChR has five potential agonist/
competitive antagonist binding sites, and at least three agonist
molecules must interact with these sites to generate a stable active
state (*33*). We also investigated the blocking and desensitizing
properties of JN403 at higher concentrations. After a full range of
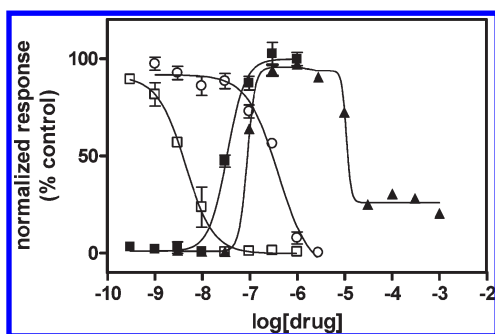

FIGURE 1: Modulation of Ca^{2+} influx in GH3 cells expressing the
human α7 AChR by agonists. Bell-shaped plot of the JN403-induced
Ca^{2+} response produced over a wide range of JN403 concentrations
($\blacktriangle$). In the lower-concentration range, JN403 stimulates the α7
AChR with practically the same efficacy but with a different potency
compared with those for ($\pm$)-epibatidine ($\blacksquare$). In the higher-concen-
tration range, JN403 inhibits the α7 AChR. In addition, cells were
pretreated with several concentrations of MLA followed by addition
of 1 μM JN403 ($\square$), or MLA was co-injected with JN403 ($\bigcirc$). The
plots are representative of 29 ($\blacksquare$), 17 ($\blacktriangle$), 8 ($\square$), and 5 ($\bigcirc$) determina-
tions, where the error bars correspond to the standard deviation.
Ligand response was normalized to the maximal ($\pm$)-epibatidine
response, which was set to 100%. The calculated EC$_{50}$, IC$_{50}$, and n_H
values for MLA and JN403 are summarized in Table 1.

JN403 concentrations [i.e., 3 nM to 1 mM (see Figure 1)] had been
tested, a bell-shaped plot was obtained showing both the stimula-
tory activity and blocking and desensitizing activity elicited by
JN403. From the inhibitory portion of the curve, an IC$_{50}$ value of
20 $\pm$ 6 μM was obtained (Table 1). Interestingly, the corresponding
n_H value was ~1, suggesting that this Ca^{2+} influx inhibition is
produced in a noncooperative manner, supporting the existence of
one binding site. This result correlates very well with a general
model in which agonists at high concentrations can block ion flux
by binding to a self-inhibitory binding site within the ion channel
(reviewed in ref *34*). However, we cannot discard a strong AChR
desensitization process at high JN403 concentrations.

The JN403-induced hα7 AChR activation was inhibited by the
specific competitive antagonist MLA using two different proto-
cols (Figure 1). The calculated IC$_{50}$ values depend on whether
MLA was preincubated (3.1 $\pm$ 0.8 nM) or co-injected with JN403
(499 $\pm$ 124 nM) (Table 1). The fact that the n_H values are higher
than unity (Table 1) indicates that the inhibitory process is
produced in a cooperative manner, suggesting the MLA interacts
with more than one binding site. This result coincides very well
with the existence of up to five agonist/competitive antagonist
sites in the α7 AChR.

*Binding Affinity of MLA and JN403 for Different
AChRs.* To compare the binding affinity of the partial agonist
JN403 for the hα7 AChR with that for the well-characterized
competitive antagonist MLA, the influence of both ligands on
binding of [^{3}H]MLA to hα7 AChRs was determined (Figure 2).
Comparing the K_i values summarized in Table 2, we demonstrate
that MLA binds to the hα7 AChR with an affinity ~5-fold higher
than that for JN403. The observed high affinity for MLA
coincides very well with its high inhibitory potency, especially
when MLA is preincubated before JN403 stimulation (Figure 2
and Table 1). The fact that the calculated n_H values are close to
unity (Table 2) indicates that JN403 and MLA inhibit [^{3}H]MLA
binding in a noncooperative manner. These data support the
general view that each ligand binds to overlapping sites within the
agonist/competitive agonist binding domain of the hα7 AChR.

To determine the receptor specificity for JN403, the affinity of
this drug for the hα7 AChR was compared to that for the hα3β4
and hα4β2 AChRs in additional radioligand binding experiments
(Figure 3). The results indicate that JN403 binds to the hα3β4

Table 1: Stimulation and Inhibition Elicited by JN403 at Different Concentrations and Inhibitory Potency of MLA Assessed by Ca^{2+} Influx in GH3-hα7 Cells

protocol	ligand	EC$_{50}$^{a}	IC$_{50}$^{b}	n_H^{c}
JN403-induced Ca^{2+} influx	JN403	103 $\pm$ 8 nM	–	2.60 $\pm$ 0.30
JN403-induced inhibition of Ca^{2+} influx at high concentrations	JN403	–	20 $\pm$ 6 μM	1.20 $\pm$ 0.21
5 min preincubation with MLA followed by activation with JN403 over several seconds	MLA	–	3.1 $\pm$ 0.8 nM	1.59 $\pm$ 0.19
co-injection of MLA and JN403 over several seconds	MLA	–	499 $\pm$ 124 nM	1.51 $\pm$ 0.05

^{a}The EC$_{50}$ value for JN403 was obtained from Figure 1. ^{b}IC$_{50}$ values were obtained from Figure 1. ^{c}Hill coefficient.

Table 2: Binding Affinity of JN403 and MLA for the hα7, hα3β4, and hα4β2 AChRs

	hα7 AChR		hα3β4 AChR		hα4β2 AChR	
ligand	K_i (nM)^a	n_H^{b}	K_i (nM)^a	n_H^{b}	K_i (nM)^a	n_H^{b}
JN403	55 $\pm$ 5	1.02 $\pm$ 0.06	2150 $\pm$ 150	0.77 $\pm$ 0.04	27700 $\pm$ 4300	0.80 $\pm$ 0.11
MLA	10 $\pm$ 1	0.77 $\pm$ 0.07	–	–	–	–

^{a}K_i values were calculated from Figure 2 ([^{3}H]MLA experiments) and Figure 3 ([^{3}H]epibatidine and [^{3}H]cytisine experiments) according to eq 2. ^{b}Hill
coefficients.
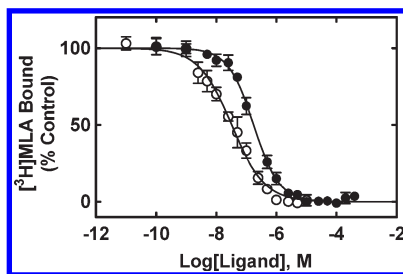
FIGURE 2: Inhibition of binding of [³H]MLA to hα7 AChRs elicited by MLA and JN403. hα7 AChR membranes prepared from SH-SY5Y-hα7 cells (1.5 mg/mL) were equilibrated (2 h) with 4 nM [³H]MLA and increasing concentrations of MLA (○) and JN403 (●). The level of nonspecific binding was determined at 10 μM MLA. Each plot is the combination of two or three separate experiments, each performed in triplicate, where the error bars correspond to the standard deviation. From these plots, the apparent IC_{50} and n_H values were obtained by a nonlinear least-squares fit according to eq 1. The K_i values were calculated using eq 2. The data are summarized in Table 2.
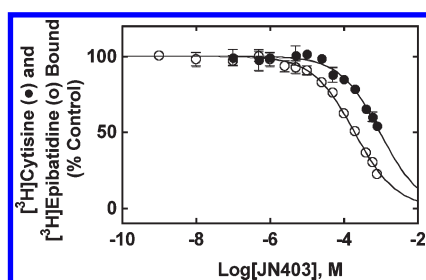

FIGURE 3: JN403-induced inhibition of binding of a radioligand agonist to hα3β4 (○) and hα4β2 (●) AChRs. AChR membranes (1.5 mg/mL) were equilibrated (2 h) with 8 nM [³H]epibatidine (○) or 9 nM [³H]cytisine (●) and increasing concentrations of JN403. The level of nonspecific binding was determined at 0.5 μM epibatidine (○) or 1 mM CCh (●). Each plot is the combination of two separate experiments, each performed in triplicate, where the error bars correspond to the standard deviation. From these plots, the apparent IC_{50} and n_H values were obtained by a nonlinear least-squares fit according to eq 1. The K_i value for JN403 was calculated using eq 2. The data are summarized in Table 2.

and hα4β2 AChRs with K_i values of 2.2 and 27.7 μM, respectively (Table 2). Consequently, the order of receptor specificity for JN403 is as follows: hα7 > hα3β4 (~40-fold) > hα4β2 (~500-fold) (Table 2). Our results are in total agreement with previous determinations (*10*).

Pharmacophores of JN403 and MLA Responsible for Receptor Binding. To determine the different structural components of JN403 and MLA that are responsible for their respective agonist and competitive antagonist properties and are responsible for the receptor selectivity of JN403, four 10 ns dynamics simulations were performed in parallel for JN403 interacting with hα7, hα3β4, and hα4β2 AChRs, and for MLA interacting with the hα7 AChR.

In our simulations, cation−π interactions were formed between the JN403 ammonium group and the aromatic cage from the hα7 (Figure 4A), hα3β4 (Figure 4B), and hα4β2 (Figure 4C) AChRs. Many hα7 AChR agonists have a cationic center that interacts with an aromatic cage at the binding cavity through cation−π interactions (e.g., see refs *35−38*). The hydrophobic cavity accommodating the aromatic ring of JN403 is also observed in the hα7 (Figure 4A), hα3β4 (Figure 4B), and hα4β2 (Figure 4C) AChRs. However, the cation−π and hydrophobic interactions between the ligand and the hα4β2 AChR
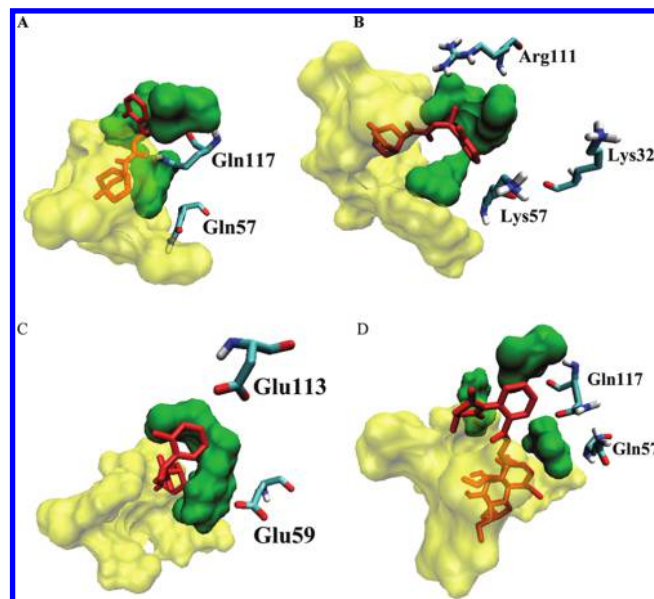
FIGURE 4: Molecular interaction of JN403 with the agonist binding site at the (A) hα7, (B) hα3β4, and (C) hα4β2 AChRs. (D) Interaction of MLA with the respective aromatic cage and hydrophobic cavity from the hα7 AChR. The aromatic cage (yellow) and the hydrophobic cavity (green) are shown as a molecular surface model, while JN403 and MLA are shown as red sticks. The figures are based on the conformation of the last frame from the molecular dynamics simulations.

were only formed at one interface, whereas JN403 diffused away from the other interfaces during the simulation (see Supporting Information 3). This is consistent with the radioligand binding results indicating that JN403 binds the hα4β2 AChR with a relatively low affinity (see Table 2). The hydrophobic cavity consists of Val108, Leu119, and Phe104 from the complementary component in the α7 subunit, whereas in the hα3β4 and hα4β2 AChRs, it is formed by Leu117, Leu119, and Ile109 from the β4 subunit and Phe117, Leu119, and Val109 from the β2 subunit. The distances between the center of mass of the aromatic ring and that of the side chains of these hydrophobic residues during the last 5 ns simulation were calculated at an interval of 10 ps, and the percentages of these distances are listed in Table 3. Considering that hydrophobic interactions occur if the distance between two groups is less than 6.5 Å, hydrophobic interactions are formed between the aromatic ring of JN403 and the hydrophobic cavities from hα7, hα3β4, and hα4β2 AChR subtypes. Although the binding cavities have similar overall shapes and constitutions among AChR subtypes (see Figure 4), the residues around them are quite different. There are two polar residues (i.e., Gln57 and Gln117) at the entrance of the hα7 AChR cavity, whereas several charged residues lie at the entrance of the hα3β4 (i.e., Lys57, Glu59, Arg111, and Lys32, from subunit β4) and hα4β2 (i.e., Glu59 and Asp113 from subunit β2) AChR cavities.

Our simulation results also indicate that JN403 has a different orientation in the hα7 AChR binding sites (Figure 4A) compared to that in the hα3β4 (Figure 4B) and hα4β2 (Figure 4C) AChRs. To compare this molecular orientation, we calculated the angles between the axis of JN403 and the axis of each pentamer at an interval of 10 ps. For the hα7 AChR, the averaged angles are 48.66 ± 8.27°, 43.76 ± 5.09°, 21.95 ± 5.54°, 38.51 ± 4.93°, and 30.25 ± 4.67° at the I_{ab}, I_{bc}, I_{cd}, I_{de}, and I_{ea} interfaces, respectively. While at the I_{bc} and I_{de} hα3β4 AChR interfaces, the averaged angles are 68.16 ± 11.55° and 68.59 ± 5.31°,

Table 3: Proportions of Residues in the Hydrophobic Cavity Interacting with the Benzene Ring from the JN403 and MLA Molecules[a]

complex	interface	Val108	Leu119	Phe104
JN403−hα7 AChR	I_{ab}	43.9%	65.1%	0
	I_{bc}	99.8%	98.6%	0
	I_{cd}	100%	100%	0
	I_{de}	99.8%	0	97.00%
	I_{ea}	100%	100%	0
MLA−hα7 AChR	I_{ab}	65.5%	0	0
	I_{bc}	0	0	0
	I_{cd}	0	0.4%	0
	I_{de}	80.0%	5.6%	0
	I_{ea}	43.5%	0	0

complex	interface	Leu117	Leu119	Ile109
JN403−hα3β4 AChR	I_{bc}	100%	100%	0.4%
	I_{de}	100%	100%	0

complex	interface	Phe117	Leu119	Val109
JN403-hα4β2 AChR	I_{bc}	0	0	0
	I_{de}	91.6%	0	65.5%

[a]The distances between the center of mass of the benzene ring from the JN403 and MLA molecules and the residue side chains in the hydrophobic cavity were calculated from the last 5 ns of the simulation at an interval of 10 ps for each ligand−receptor complex. The residues that have a distance of < 6.5 Å were defined as residues interacting with the ligand.
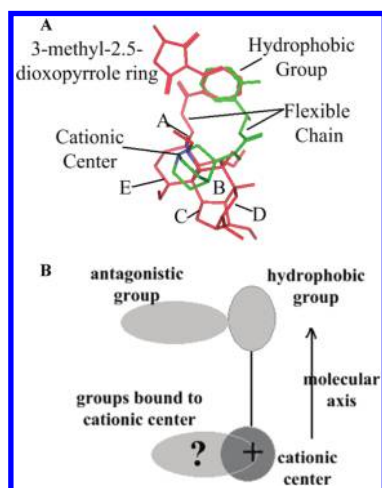

FIGURE 5: Possible pharmacophores for the α7 AChR binding site. (A) Molecular alignment of MLA (red) with JN403 (green). The nitrogen atom from the cationic center is colored blue, and the MLA rings are named A−E. (B) Possible pharmacophore model for α7 AChR antagonists. MLA has an ammonium group as a cationic center and a benzene ring as a hydrophobic group. These two moieties connected by a flexible chain at a distance of ∼8−9 Å are required for ligand binding. An additional group connected to the hydrophobic moiety and extending perpendicular to the molecular axis is responsible for its antagonistic property. This latter group should not contain any charges from the surrounding residues where aromatic residues are located, and it should have a width of at least 5−6 Å.

respectively. The angle for the I_{de} interface in the hα4β2 AChR is 53.81 ± 5.23°, a value between those determined for the hα7 and hα3β4 AChRs. The difference between the hα7 and hα3β4 AChRs could be attributed to the distinct relative positions between the aromatic cage and the hydrophobic cavity in the hα7 AChR compared to that in the hα3β4 AChR.

Figure 5A shows that MLA, a specific and potent competitive antagonist of α7 AChRs, has two similar structural components when compared to JN403: a cationic center and a hydrophobic group, both connected by a relatively flexible chain. The distance between the cationic center and the center of mass of the hydrophobic group is 8−9 Å for both molecules. In addition, the conformation of rings A and E from the MLA molecule also resembles the conformation of the carbon atoms connected to the ammonium nitrogen (i.e., carbon cage) in the JN403 molecule (see the molecular comparison in Figure 5A). The hydrophobic interaction between the hydrophobic group from MLA and the hydrophobic cavity from the complementary component was also analyzed, and the results are shown in Table 3. These data proved the existence of cation−π and hydrophobic interactions between MLA and the hα7 AChR (see Figure 4D). JN403 forms hydrophobic interactions with the hydrophobic cavity in each subunit interface, whereas MLA forms hydrophobic interactions only at the I_{ab}, I_{de}, and I_{ea} interfaces (Table 3).

Our experiments support previous results indicating the existence of two important AChR domains for ligand binding, i.e., an aromatic cage and a hydrophobic cavity. These two domains interact with the most significant pharmacophores responsible for the binding of both agonists (i.e., JN403) and antagonists (i.e., MLA). More specifically, our results indicate that the ligand cationic center (i.e., ammonium group) forms cation−π interactions with the aromatic cage, whereas the ligand hydrophobic group (i.e., aromatic ring) forms hydrophobic interactions with the hydrophobic cavity. We speculated that this model is universal in different AChR types and plays a key role for both agonist and antagonist binding.

Hydrogen Bond Interactions between Ligands and AChRs. We first determined the average number of hydrogen bonds formed between JN403 and each subunit interface (i.e., α7−α7, α3−β4, and α4−β2) in the last 5 ns of the simulation calculated at an interval of 10 ps. The numbers of hydrogen bonds were 0.49, 0.66, 1.11, 1.54, and 1.58 at the I_{ab}, I_{bc}, I_{cd}, I_{de}, and I_{ea} interfaces of the hα7 AChR, respectively, while at the I_{bc} and I_{de} interfaces of the hα3β4 AChR, the numbers of hydrogen bonds were 0.18 and 0.35, respectively. The corresponding number at one α4−β2 interface was 0.59 [the hydrogen bonds at the other interfaces were not analyzed since JN403 diffused away from the binding

cavity (see Supporting Information 3)]. In general, these results indicate weaker hydrogen bond interactions between JN403 and the hα3β4 and hα4β2 AChRs, compared with that for the hα7 AChR.

The averaged numbers of hydrogen bonds between MLA and hα7 AChR were also calculated with the same method: 2.57, 1.46, 1.58, 2.48, and 2.74 for each of the five subunit interfaces. This result indicates that MLA forms more hydrogen bonds with the hα7 AChR binding sites than JN403, which is rationalized by the fact that MLA has more polar atoms (such as oxygen) than the JN403 molecule. This supports the observed higher affinity of MLA for the hα7 AChR compared with that of JN403 (Table 2).

Although the hydrogen bonds formed depend on the receptor and the specific interface, a consistent model of the hydrogen bonds was found for the hα7 and hα3β4 AChRs (see Supporting Information 4). The nitrogen atoms from the ammonium (N^+) and carbamate (NH) groups from JN403 are the most important structural components for hydrogen bond interactions between the ligand and the AChRs. More specifically, residues Trp149, Tyr93, and Tyr195 from the hα7 AChR aromatic cage and Trp146 and Tyr90 from the hα3β4 AChR aromatic cage are pivotal components for the formation of hydrogen bonds. The hydrogen bond analysis also indicates that the hydrogen bonds formed between JN403 and the hα3β4 AChR are much weaker that those for the hα7 AChR (see Supporting Information 4), which may be responsible for the determined lower affinity of JN403 for the hα3β4 AChR (see Table 2). We infer that this difference is the result of the distinct relative position of the aromatic cage and hydrophobic cavity in the hα3β4 AChR compared to that in the hα7 AChR. This different position changes the orientation of the JN403 molecule, affecting the conformation of the ammonium and carbamate groups in the aromatic cage and, hence, weakening the hydrogen bonds in the hα3β4 AChR, especially that between the NH atom and the Trp146 O atom (see Supporting Information 4). The oxygen atoms in the hα3β4 AChR also formed fewer hydrogen bonds than those in the hα7 AChR, which may be attributed to a more hydrophobic environment of the hα3β4 (e.g., α7-Gln117 mutated to β4-Leu117) AChR binding cavity. Interestingly, the hydrogen bond model described in the JN403−hα3β4 AChR and JN403−hα7 AChR complexes was not found in the JN403−hα4β2 AChR complex. In this case, hydrogen bonds are formed between the ammonium from JN403 and the oxygen from the backbone of α4-Trp147 and between the carbamate group and the oxygen from the α4-Tyr195 side chain. The averaged number of hydrogen bonds (~0.6 in the hα4β2 AChR compared to ~1.1 in the hα7 AChR) also indicates weaker hydrogen bond interactions between JN403 and the hα4β2 AChR.

Our hydrogen bond analysis reveals that, in addition to the previously determined pharmacophores for JN403 (i.e., ammonium group and hydrophobic ring), its carbamate group can be considered another pharmacophore. We also speculated that the different orientation of JN403 in the hα3β4 AChR compared to that in the hα7 AChR weakens the hydrogen bond between the carbamate group and α3-Trp146. This structural feature and the smaller number of hydrogen bonds between JN403 and the hα3β4 and hα4β2 AChRs compared to that for the hα7 AChR might be responsible for the observed receptor selectivity of JN403 (see Table 2).

Different hα7 AChR Motions Induced by JN403 and MLA. The MLA molecule has two additional structural moieties that are not equivalent in the JN403 molecule: the 3-methyl-2,5-dioxopyrrole ring that is connected to the hydrophobic group and
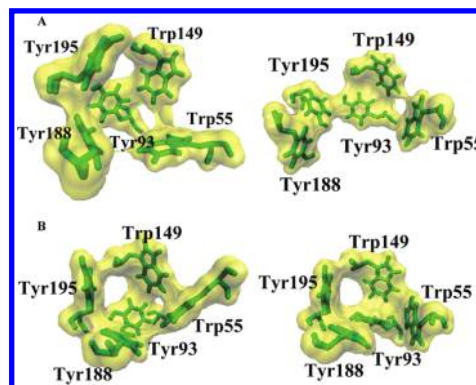

FIGURE 6: Molecular surface model (yellow) of the aromatic cage in the binding cavity of the (A) MLA−hα7 AChR and (B) JN403−hα7 AChR complexes. The left and right models show the ligand−hα7 AChR complex before and after the 10 ns dynamics simulation, respectively. The aromatic cage of the hα7 AChR was disabled after MLA binding, whereas that for the JN403−hα7 AChR complex remained unaltered. The most important amino acids are shown as green stick models.

the B−D rings (see Figure 5A) that are connected together with several oxygen atoms located at different positions around them. The simulation results for the JN403−hα7 AChR and MLA−hα7 AChR complexes revealed that the motion of the AChR binding cavity depends on the type of bound ligand and that this motion is distributed throughout the protein (see Supporting Information 5I−III). We also determined that the 3-methyl-2,5-dioxopyrrole ring and the B−D rings are important for its antagonistic properties. The ammonium nitrogen of MLA was positioned in the hα7 AChR aromatic cage, with the hydrogen and the ethyl group, which is connected to the nitrogen, pointing to the Trp149 residue. However, this aromatic cage, which accommodates the cationic center of the JN403 molecule, was disabled by the MLA molecule during the simulation (see Figure 6A). For JN403, the aromatic cage remains unaltered during the 10 ns simulation (see Figure 6B), whereas for MLA, both Tyr195 and Tyr188 are pushed away by the 3-methyl-2,5-dioxopyrrole ring and the B−D rings and the aromatic cage was disabled (see Figure 6A).

We next analyzed the motion of the protein in the MLA− and JN403−ha7 AChR complexes (see Supporting Information 5). When the agonist binds to the protein, loop C (see Supporting Information 1) was inclined to move inward, occluding the entrance of the cavity, while the antagonist molecule pushed loop C away (see Supporting Information 5II). The motion of loop C causes a rotation of the β-sandwich, inducing a motion of the Cys loop and β_1-β_2 loop which interact with the M2 helices from the transmembrane domain. The rotation of the β-sandwich was observed only in subunit *d* in our 10 ns simulation (see Supporting Information 5II), whereas a similar conformational change was observed in subunit *b* when the simulations were extended to 15 ns. To explain this motional difference, we suggest that the relatively larger molecular volume of MLA (~760 Å^3) is responsible for the different motions observed in loop C. To orient the MLA ammonium group in the aromatic cage to form the cation−π interaction, loop C must be pushed away by steric hindrance with the bulky group (i.e., the 3-methyl-2,5-dioxopyrrole ring and the B−D rings) around the nitrogen, while the space in the aromatic cage is large enough to accommodate the JN403 ammonium group (JN403 molecular volume of 340 Å^3). The average distances between the center of mass of the 3-methyl-2,5-dioxopyrrole ring from the MLA molecule and that of Tyr195

Table 4: Results of the Free Energy Calculation for JN403 at the $\alpha7-\alpha7$, $\alpha3-\beta4$, and $\alpha4-\beta2$ Interfaces[a]

| | energy terms (kcal/mol) | | | | | $\Delta G + TS_{MM}$ (kcal/mol) | |
interface	ΔE_{ele}	ΔE_{vdw}	$\Delta G_{nonpolar}$	$\Delta G_{PBSA-polar}$	$\Delta G_{GBSA-polar}$	PBSA	GBSA
$\alpha7-\alpha7$	-167.9 ± 6.5	-43.3 ± 1.9	-5.5 ± 0.2	185.8 ± 6.5	170.6 ± 7.1	-30.8 ± 3.3	-46.0 ± 2.8
$\alpha3-\beta4$	-143.1 ± 7.5	-38.9 ± 2.1	-5.5 ± 0.1	161.8 ± 7.1	149.1 ± 7.5	-25.6 ± 4.1	-38.3 ± 2.9
$\alpha4-\beta2$	-230.5 ± 6.0	-32.4 ± 1.8	-5.1 ± 0.2	247.5 ± 4.5	235.9 ± 5.1	-20.5 ± 3.5	-32.2 ± 2.6

[a]Binding free energy was calculated by both MM-PBSA and MM-GBSA methods. ΔE_{ele}, ΔE_{vdw}, $\Delta G_{nonpolar}$, $\Delta G_{PBSA-polar}$, $\Delta G_{GBSA-polar}$, PBSA, and GBSA denote changes in the electrostatic interaction energy, the van der Waals interaction energy, the nonpolar solvation energy, the polar solvation energy determined by the MM-PBSA method, the polar solvation determined by the MM-GBSA method, the total energy determined by the MM-PBSA method, and the total energy determined by the MM-GBSA method during the process of ligand binding, respectively. Since a single-trajectory method was used during the calculation, the changes in the ΔE_{int} terms are zero and, thus, are not listed here.

during the last 5 ns of the simulations were 6.55 ± 0.32, 12.40 ± 0.36, 9.92 ± 0.65, 5.48 ± 0.62, and 12.55 ± 0.91 Å at the I_{ab}, I_{bc}, I_{cd}, I_{de}, and I_{ea} interfaces, respectively. This result indicates a possible interaction between these two groups at the I_{ab}, I_{cd}, and I_{de} interfaces.

The antagonist MLA induces different motions on loop C by pushing Tyr195 and Tyr188 away from the binding cavity (see Supporting Information 5III). During the simulation, MLA remained in a conformation where the 3-methyl-2,5-dioxopyrrole ring was oriented nearly perpendicular to the flexible chain connecting the cationic center and the hydrophobic group. In this conformation, the 3-methyl-2,5-dioxopyrrole ring pointed toward the Tyr195 side chain and pushed it away. Since Tyr188 lies at the bottom of the aromatic cage in the hα7 AChR−JN403 complex and the B−D rings extend toward the bottom of the cage during the MLA−hα7 AChR complex simulation, the conformational change of Tyr188 may be attributed to the B−D rings. On the basis of our simulation trajectories, we infer that the bulky moiety formed by the 3-methyl-2,5-dioxopyrrole ring and the B−D rings around the protonated nitrogen of MLA is the most important structural feature that supports its antagonistic property by pushing loop C away. In this regard, the ammonium group, which forms cation−π interactions with the aromatic cage of the binding cavity, as well as the benzene ring, which forms hydrophobic interaction with the complementary component, can be considered pharmacophores for both agonists and antagonists.

Receptor Selectivity for JN403 Assessed by Free Energy Calculation and Computational Ala Scanning. To compare the binding affinity of JN403 between the hα7 and hα3β4 and hα4β2 AChRs, and to confirm the role of the residues shown to be important in ligand binding by dynamics simulations, we conducted free energy calculations (Table 4) and Ala scanning simulations (see Supporting Information 6) for JN403 at the $\alpha7-\alpha7$, $\alpha3-\beta4$, and $\alpha4-\beta2$ interfaces. Both MM-PBSA and MM-GBSA methods indicated that JN403 has a much lower binding free energy when interacting with the hα7 AChR compared to that for the hα3β4 and hα4β2 AChRs (see Table 4), consistent with the experimental results (see Table 2). The lower binding free energy of JN403 for the $\alpha7-\alpha7$ interface can be attributed to both a weaker electrostatic interaction (ΔE_{ele}) and especially a weaker van der Waals interaction (ΔE_{vdw}). Although the ΔE_{ele} term of JN403 for the hα7 AChR was much lower (-167.9 kcal/mol) than that for the hα3β4 AChR (-143.1 kcal/mol), the total electrostatic contribution (including the contribution from molecular mechanics energy and the polar solvation energy, i.e., the sum of ΔE_{ele} and $\Delta G_{PBSA/GBSA-polar}$) to the binding free energy was only slightly smaller in the hα7 AChR

(a difference of 0.9 kcal/mol by the MM-PBSA method and of 3.3 kcal/mol by the MM-GBSA method). The latter is probably due to higher polar solvation energy for the hα7 AChR−JN403 complex compared to that for the hα3β4 AChR−JN403 complex. The JN403 molecule has a lower van der Waals interaction energy when binding to the hα7 AChR compared to that for the hα3β4 AChR (a difference of 4.4 kcal/mol). Interestingly, the condition for the hα4β2 AChR−JN403 complex is different. JN403 has a stronger electrostatic interaction (ΔE_{ele}, a difference of 62.6 kcal/mol) and weaker van der Waals interaction (ΔE_{vdw}, a difference of 10.9 kcal/mol) with the $\alpha4-\beta2$ interface compared to those with the $\alpha7-\alpha7$ interface (Table 4). Hence, the difference in free energy (and the difference in binding affinity) between the $\alpha4-\beta2$ interface and the $\alpha7-\alpha7$ interface is mainly attributed to the different van der Waals energies.

The molecular dynamics simulations predicted that there are several charged residues around the hydrophobic cavity in the hα3β4 AChR (e.g., Lys32, Lys57, Glu59, and Arg111), whereas most of the residues around the hydrophobic cavity in the hα7 AChR are not charged (e.g., Gln57 and Gln117). The mutation of the positively charged residues in the β4 subunit (i.e., Lys32, Lys57, and Arg111) greatly weakens the electrostatic interaction (i.e., the ΔE_{ele} term), while the mutation of the negatively charged residue Glu59 increases this value (Supporting Information 6, Table A). This result suggests that positive charges are unfavorable elements for the molecular binding between JN403 and the hα3β4 AChR. This is consistent with the fact that the hα7 AChR pentamer is more negatively charged (-20) than the hα3β4 AChR pentamer (-13). This difference is obtained considering that the net negative charges of the α7, α3, and β4 subunits are -4, -5, and -1, respectively. Since the pK_a of JN403 is 10.3 (obtained according to the method of ref *40*), $\sim$99.9% is in the protonated form at physiological pH, and thus, the net negative charge in the hα7 AChR pentamer favors ligand binding. Hence, the net charge of the AChR pentamer is another possible element responsible for the observed agonist selectivity. Positively charged residues around the AChR binding cavity may be also responsible for drug selectivity. The MM-PBSA/GBSA methods predicted quite different total free energy changes for the Ala mutations of the amino acids surrounding the hα3β4 (Table A) and hα7 (Table B) AChR binding pockets (see Supporting Information 6). These differences came from the different polar solvation energies predicted by these two methods. We speculated that the mutation of these residues to polar residues will greatly decrease the electrostatic interaction energy and induce smaller changes in the polar solvation energy, resulting in a lower binding affinity of JN403 for the hα3β4 AChR. The Gln57Ala mutation in the α7 subunit did not change the free energy,

whereas the Gln117Ala mutation increases both ΔE_{ele} and ΔE_{vdw} terms (Table B). Thus, α7-Gln117 is proven to play a key role in ligand binding. Additional results for the hα3β4 AChR indicate that the closer the residue to the binding site, the greater the decrease in the electrostatic interaction energy induced by its mutation. For example, ΔE_{ele} decreased by 43.5, 29.5, and 21.5 kcal/mol for the Lys57Ala, Arg111Ala, and Lys32Ala mutations, respectively, while Lys57 is the nearest to the binding cavity, Arg111 is more distant, and Lys32 is the most distant. Thus, not only the net charge of the subunit interface but also the relative positions of the positively charged residues can affect the binding affinity of the ligand. Ala mutations of the amino acids surrounding the hα4β2 binding site (Table C) indicate that cation–π and hydrophobic interactions were both formed between hα4β2 and JN403 (see Supporting Information 6).

As indicated previously (see Table 4), the higher binding free energy of JN403 in the α4–β2 interface was not attributed to the electrostatic interaction but to the unfavorable van der Waals interaction. The hα4β2 AChR pentamer is more negatively charged ($-$37) than the hα7 AChR pentamer ($-$20); hence, JN403, which is positively charged, should have a higher binding affinity with the hα4β2 AChR considering only the electrostatic interaction. However, the van der Waals interaction energy (ΔE_{vdw}) between JN403 and the α4–β2 interface showed a very unfavorable van der Waals interaction. This is why the obtained total free energy indicates that the binding between JN403 and the α7–α7 interface is more favorable than that between JN403 and the α4–β2 interface, which is consistent with the experimental results (Table 2). In fact, the order of the total free energy (kilocalories per mole) obtained by the MM-GBSA method for the three AChRs is as follows: -46.0 ± 2.8 (hα7) $> -38.3 \pm 2.9$ (hα3β4) $> -32.2 \pm 2.6$ (hα4β2).

DISCUSSION

An important objective of this work is to characterize the pharmacophore for agonists and antagonists of the hα7 AChR. In this regard, the binding, functional, and specificity properties of JN403 were determined on the hα7, hα3β4, and hα4β2 AChRs. We applied a variety of approaches, including radioligand binding assays, Ca^{2+} influx detections, and molecular docking and dynamics studies.

To determine the inhibitory potency of MLA on JN403-activated Ca^{2+} influx in GH3-hα7 cells, we used preincubation and co-injection protocols (Figure 1). The results indicated that MLA inhibits the JN403-activated hα7 AChR with potencies that depend on the used protocol (Table 1). A potential explanation for the observation that MLA preincubation inhibits the hα7 AChR with a potency 160-fold higher than that determined by co-injection with JN403 is that MLA binds with high affinity to the resting hα7 AChR and stabilizes this conformational state, thus decreasing the likelihood of the subsequent JN403-induced AChR activation. Another alternative explanation is that the interaction of MLA with the resting hα7 AChR increases the desensitization rate, precluding the agonist-induced Ca^{2+} influx. Although we cannot distinguish between these two different inhibitory mechanisms, our first proposed model fits very well with previous observations where MLA inhibits the spontaneous activity of the Leu247Thr α7 AChR mutant (*39*).

The results from the radioligand competition binding experiments indicate that MLA binds to the hα7 AChR with an affinity ~5-fold higher than that for JN403 (see Table 2), which coincides

with the high inhibitory potency of this ligand (Table 1). The molecular dynamics simulations of the JN403–hα7 AChR and MLA–hα7 AChR complexes indicate that the ligand-induced loop C motion depends on the ligand type (see Supporting Information 5). In the antagonist-bound receptor, the bulky moiety [i.e., the 3-methyl-2,5-dioxopyrrole ring and the B–D rings (see Figure 5A)] around the ammonium group pushes away the Tyr195 and Tyr188 residues that lay on loop C, outward from the center of the pentamer barrel, while JN403 draws loop C inward. The motion of the MLA-bound receptor in our simulation is similar to that determined for ligands binding to the AChBP (*40*, *41*). Hence, we speculated that MLA changes the conformation of loop C, inducing a rotation of the β-sandwich and a conformational change in the Cys loop, finally stabilizing the hα7 AChR in the resting state. We also found that the distance between the 3-methyl-2,5-dioxopyrrole ring and Tyr195 is quite short, and consequently, Tyr195 may be pushed away by the ring, supporting the notion that the 3-methyl-2,5-dioxopyrrole ring is responsible for the antagonist activity of MLA by a steric hindrance mechanism. This conclusion is consistent with the fact that the antagonistic action of MLA is completely lost if the ring is removed from the molecule (*42*). Since the B–D rings, which are connected to the cationic center of MLA, lie in the aromatic cage, and their volume is relatively large compared to the size of the aromatic cage, we speculated that this moiety also contributes to the structural distortion of the aromatic cage by steric hindrance. The cationic center and the aromatic ring are pharmacophores for both MLA and JN403, playing key roles in the binding process, whereas the 3-methyl-2,5-dioxopyrrole ring and the B–D rings are the most probable structural components responsible for the antagonist activity of MLA. Considering the conformation of MLA in our simulation (see Figures 4C and 6A), a possible pharmacophore model for hα7 AChR antagonists is proposed (see Figure 5B): a cationic center and a hydrophobic group separated by ~8–9 Å are required for ligand binding, and an additional group extending perpendicular to the molecule axis is necessary for the antagonistic property. This latter group should not contain any charges because the surrounding residues are uncharged residues such as aromatic residues (e.g., Tyr), and it should have a width of at least 5–6 Å.

The radioligand competition binding experiments also indicate that the order of receptor specificity for JN403 is as follows: hα7 $>$ hα3β4 (~40-fold) $>$ hα4β2 (~500-fold). This specificity is based on the natural residue mutations observed among the different AChR binding sites (see Supporting Information 2). Although the hα3β4 and hα4β2 AChR binding domains have structural characteristics similar to those found in the hα7 AChR (see Figure 4), there are several important distinctions that result in the observed receptor specificity. The most important follow.

(a) Three residues surrounding the hα3β4 binding cavity are positively charged, producing electrostatic repulsion with JN403 (see Supporting Information 6), which is also positively charged at physiological pH (~99.9%).

(b) The orientation of the JN403 molecule in the hα3β4 AChR binding sites is different from that for the hα7 AChR, producing fewer hydrogen bonds in the JN403–hα3β4 AChR complex compared to the number in the JN403–hα7 AChR complex.

(c) The hα3β4 pentamer is less negatively charged ($-$13) than the hα7 pentamer ($-$20), producing a weaker electrostatic interaction with JN403 when compared to that for the hα7 AChR. This result is consistent with the studies by Huang et al. (*43*),

who argued that long-range electrostatic interactions play a key role in ligand selectivity for the hα4β2 AChR.

(d) For the case of the hα4β2 pentamer, unfavorable van der Waals interactions have been calculated for JN403, resulting in lower free energy values compared to that for the hα7 AChR (Table 4).

In conclusion, the combination of different electrostatic and van der Waals interactions may explain the higher receptor specificity of JN403 for the hα7 AChR determined by radioligand binding assays (see Table 2).

Collectively, our results indicate that (1) there are two pharmacophores (i.e., a cationic center and a hydrophobic group) important for agonist (i.e., JN403) and competitive antagonist (i.e., MLA) binding (the cationic center and the hydrophobic group interact with the aromatic cage and the hydrophobic cavity, respectively, found in different AChRs); (2) the carbamate group in JN403 is another pharmacophore important for its agonist activity, by forming hydrogen bonds with the hα3β4 and hα7 AChRs; (3) the determined higher specificity of JN403 for the hα7 AChR compared to that for the hα3β4 and hα4β2 AChRs is due to an electrostatic repulsion between positively charged residues surrounding the hα3β4 binding cavity and the cationic center in JN403, fewer hydrogen bonds for the interaction of JN403 with the hα3β4 AChR, and unfavorable van der Waals interactions of JN403 with the hα4β2 binding cavity; and (4) the 3-methyl-2,5-dioxopyrrole ring and the B–D rings are responsible for the competitive antagonistic property of MLA.

ACKNOWLEDGMENT

SUPPORTING INFORMATION AVAILABLE

Additional experimental observations. This material is available free of charge via the Internet at http://pubs.acs.org.

REFERENCES

1. Arias, H. R. (2006) Ligand-gated ion channel receptor superfamilies. In Biological and Biophysical Aspects of Ligand-Gated Ion Channel Receptor Superfamilies (Arias, H. R., Ed.) pp 1–25, Research Signpost, Kerala, India.
2. Albuquerque, E. X., Pereira, E. F. R., Alkondon, A., and Rogers, S. W. (2009) Mammalian nicotinic acetylcholine receptors: From structure to function. *Physiol. Rev. 89*, 73–120.
3. Romanelli, M. N., Gratteri, P., Guandalini, L., Martini, E., Bonaccini, C., and Gualtieri, F. (2007) Central nicotinic receptors: Structure, function, ligands, and therapeutic potential. *ChemInform 2*, 746–767.
4. Arias, H. R., Richards, V., Ng, D., Ghafoori, M. E., Le, V., and Mousa, S. (2009) Role of non-neuronal nicotinic acetylcholine receptors in angiogenesis. *Int. J. Biochem. Cell Biol. 41*, 1441–1451.
5. Tuppo, E. E., and Arias, H. R. (2005) The role of inflammation in Alzheimer's disease. *Int. J. Biochem. Cell Biol. 37*, 289–305.
6. Arias, H. R. (2009) Is the inhibition of nicotinic acetylcholine receptors by bupropion involved in its clinical actions? *Int. J. Biochem. Cell Biol. 41*, 2098–2108.
7. Arias, H. R. (1997) Topology of ligand binding sites on the nicotinic acetylcholine receptor. *Brain Res. Rev. 25*, 133–191.
8. Ellison, M., and Olivera, B. M. (2007) α4/3 Conotoxins: Phylogenetic distribution, functional properties, and structure-function insights. *Chem. Rec. 7*, 341–353.
9. Davies, A. R., Hardick, D. J., Blagbrough, I. S., Potter, B. V., Wolstenholme, A. J., and Wonnacott, S. (1999) Characterisation of the binding of [^{3}H]methyllycaconitine: A new radioligand for labelling α7-type neuronal nicotinic acetylcholine receptors. *Neuropharmacology 38*, 679–690.
10. Feuerbach, D., Nozulak, J., Lingenhoehl, K., McAllister, K., and Hoyer, D. (2007) JN403, *in vitro* characterization of a novel nicotinic acetylcholine receptor α7 selective agonist. *Neurosci. Lett. 416*, 61–65.
11. Feuerbach, D., Lingenhoehl, K., Olpe, H. R., Vassout, A., Gentsch, C., Chaperon, F., Nozulak, J., Enz, A., Bilbe, G., McAllister, K., and Hoyer, D. (2009) The selective nicotinic acetylcholine receptor α7 agonist JN403 is active in animal models of cognition, sensory gating, epilepsy and pain. *Neuropharmacology 56*, 254–263.
12. Arias, H. R., Xing, H., MacDougall, K., Blanton, M. P., Soti, F., and Kem, W. R. (2009) Interaction of benzylidene-anabaseine analogs with agonist and allosteric sites on muscle nicotinic acetylcholine receptors. *Br. J. Pharmacol. 157*, 320–330.
13. Wei, D.-Q., Sirois, S., Du, Q.-S., Arias, H. R., and Chou, K.-C. (2005) Theoretical studies of Alzheimer's disease drug candidate 3-[(2,4-dimethoxy)benzylidene]-anabaseine (GTS-21) and its derivatives. *Biochem. Biophys. Res. Commun. 338*, 1059–1064.
14. Kem, W. R., Soti, F., LeFrancois, S., Wildeboer, K., MacDougall, K., Wei, D.-Q., Chou, K.-C., and Arias, H. R. (2006) The nemertine toxin anabaseine and its derivative DMXBA (GTS-21): Chemical and pharmacological properties. *Mar. Drugs 4* (Special Issue: Marine Toxins and Ion Channels), 255–273.
15. Enz, A., Feuerbach, D., Frederiksen, M. U., Gentsch, C., Hurth, K., Müller, W., Nozulak, J., and Roy, B. L. (2009) γ-Lactams: A novel scaffold for highly potent and selective α7 nicotinic acetylcholine receptor agonists. *Bioorg. Med. Chem. Lett. 19*, 1287–1291.
16. Michelmore, S., Croskery, K., Nozulak, J., Hoyer, D., Longato, R., Weber, A., Bouhelal, R., and Feuerbach, D. (2002) Study of the calcium dynamics of the human α4β2, α3β4 and α1β1$\gamma$$\delta$ nicotinic acetylcholine receptors. *Naunyn-Schmiedeberg's Arch. Pharmacol. 366*, 235–245.
17. Feuerbach, D., Lingenhohl, K., Dobbins, P., Mosbacher, J., Corbett, N., Nozulak, J., and Hoyer, D. (2005) Coupling of human nicotinic acetylcholine receptors α7 to calcium channels in GH3 cells. *Neuropharmacology 48*, 215–227.
18. Charpantier, E., Wiesner, A., Huh, K.-H., Ogier, R., Hoda, J.-C., Allman, G., Raggenbass, M., Feuerbach, D., Bertrand, D., and Fuhrer, C. (2005) α7 neuronal nicotinic acetylcholine receptors are negatively regulated by tyrosine phosphorylation and src-family kinases. *J. Neurosci. 25*, 9836–9849.
19. Arias, H. R., Feuerbach, D., Bhumireddy, P., and Ortells, M. O. (2010) Inhibitory mechanisms and binding site locations for serotonin selective reuptake inhibitors on nicotinic acetylcholine receptors. *Int. J. Biochem. Cell Biol. 42*, 712–724.
20. Arias, H. R., Targowska-Duda, K. M., Sullivan, C. J., Feuerbach, D., Maciejewski, R., and Jozwiak, K. (2010) Different interaction between tricyclic antidepressants and mecamylamine with the human α3β4 nicotinic acetylcholine receptor. *Int. Neurochem. 56*, 642–649.
21. Cheng, Y., and Prusoff, W. H. (1973) Relationship between the inhibition constant (K_i) and the concentration of inhibitor which causes 50% inhibition (IC_{50}) of an enzymatic reaction. *Biochem. Pharmacol. 22*, 3099–3108.
22. Zhang, J., and Steinbach, J. H. (2003) Cytisine binds with similar affinity to nicotinic α4β2 receptors on the cell surface and in homogenates. *Brain Res. 959*, 98–102.
23. Chou, K.-C. (2004) Insights from modelling the 3D structure of the extracellular domain of α7 nicotinic acetylcholine receptor. *Biochem. Biophys. Res. Commun. 319*, 433–438.
24. Brejc, K., Van Dijk, W. J., Klaassen, R. V., Schuurmans, M., Van Der Oost, J., Smit, A. B., and Sixma, T. K. (2001) Crystal structure of an ACh-binding protein reveals the ligand-binding domain of nicotinic receptors. *Nature 411*, 269–276.
25. Unwin, N. (2005) Refined structure of the nicotinic acetylcholine receptor at 4 Å resolution. *J. Mol. Biol. 346*, 967–989.
26. Morris, G. M., Goodsell, D. S., Halliday, R. S., Huey, R., Hart, W. E., Belew, R. K., and Olson, A. J. (1998) Automated docking using a Lamarckian genetic algorithm and an empirical binding free energy function. *J. Comput. Chem. 19*, 1639–1662.
27. Lindahl, E., Hess, B., and Van Der Spoel, D. (2001) GROMACS: A package for molecular simulation and trajectory analysis. *J. Mol. Model. 7*, 306–317.
28. Hess, B., Bekker, H., Berendsen, H. J. C., and Fraaije, J. (1997) LINCS: A linear constraint solver for molecular simulations. *J. Comput. Chem. 18*, 1463–1472.
29. Kollman, P. A., Massova, I., Reyes, C., Kuhn, B., Huo, S., Chong, L., Lee, M., Lee, T., Duan, Y., Wang, W., Donini, O., Cieplak, P., Srinivasan, J., Case, D. A., and Cheatham, T. E. (2000) Calculating structures and free energies of complex molecules: Combining molecular mechanics and continuum models. *Acc. Chem. Res. 33*, 889–897.

30. Grazioso, G., Cavalli, A., De Amici, M., Recanatini, M., and De Micheli, C. (2008) α7 nicotinic acetylcholine receptor agonists: Prediction of their binding affinity through a Molecular Mechanics Poisson-Boltzmann Surface Area approach. *J. Comput. Chem. 29*, 2593–2603.

31. Pearlman, D. A., Case, D. A., Caldwell, J. W., Ross, W. S., Cheatham, T. E., III, DeBolt, S., Ferguson, D., Seibel, G., and Kollman, P. (1995) AMBER, a package of computer programs for applying molecular mechanics, normal mode analysis, molecular dynamics and free energy calculations to simulate the structural and energetic properties of molecules. *Comput. Phys. Commun. 91*, 1–41.

32. Massova, I., and Kollman, P. A. (1999) Computational alanine scanning to probe protein-protein interactions: A novel approach to evaluate binding free energies. *J. Am. Chem. Soc. 121*, 8133–8143.

33. Rayes, D., De Rosa, M. J., Sine, S. M., and Bouzat, C. (2009) Number and locations of agonist binding sites required to activate homomeric Cys-loop receptors. *J. Neurosci. 29*, 6022–6032.

34. Arias, H. R. (1996) Agonist self-inhibitory binding site of the nicotinic acetylcholine receptor. *J. Neurosci. Res. 44*, 97–105.

35. Beene, D. L., Brandt, G. S., Zhong, W., Zacharias, N. M., Lester, H. A., and Dougherty, D. A. (2002) Cation-π interactions in ligand recognition by serotonergic (5-HT$_{3A}$) and nicotinic acetylcholine receptors: The anomalous binding properties of nicotine. *Biochemistry 41*, 10262–10269.

36. Ma, J. C., and Dougherty, D. A. (1997) The cation-π interaction. *Chem. Rev. 97*, 1303–1324.

37. Henchman, R. H., Wang, H.-L., Sine, S. M., Taylor, P., and McCammon, J. A. (2005) Ligand-induced conformational change in the α7 nicotinic receptor ligand binding domain. *Biophys. J. 88*, 2564–2576.

38. Lester, H. A., Dibas, M. I., Dahan, D. S., Leite, J. F., and Dougherty, D. A. (2004) Cys-loop receptors: New twists and turns. *Trends Neurosci. 27*, 329–336.

39. Bertrand, S., Devillers-Thiéry, A., Palma, E., Buisson, B., Edelstein, S. J., Corringer, P. J., Changeux, J. P., and Bertrand, D. (1997) Paradoxical allosteric effects of competitive inhibitors on neuronal α7 nicotinic receptor mutants. *NeuroReport 8*, 3591–3596.

40. Gao, F., Bren, N., Burghardt, T. P., Hansen, S., Henchman, R. H., Taylor, P., McCammon, J. A., and Sine, S. M. (2005) Agonist-mediated conformational changes in acetylcholine-binding protein revealed by simulation and intrinsic tryptophan fluorescence. *J. Biol. Chem. 280*, 8443–8451.

41. Ulens, C., Akdemir, A., Jongejan, A., Van Elk, R., Bertrand, S., Perrakis, A., Leurs, R., Smit, A. B., Sixma, T. K., Bertrand, D., and De Esch, J. P. (2009) Use of acetylcholine binding protein in the search for novel α7 nicotinic receptor ligands. *In silico* docking, pharmacological screening, and X-ray analysis. *J. Med. Chem. 52*, 2372–2383.

42. Baker, D., Brimble, M. A., McLeod, M. D., and Savage, G. P. (2004) Synthesis of tricyclic analogues of methyllycaconitine using ring closing metathesis to append a B ring to an AE azabicyclic fragment. *Org. Biomol. Chem. 2*, 1659–1669.

43. Huang, X., Zheng, F., Chen, X., Crooks, P. A., Dwoskin, L. P., and Zhan., C. G. (2006) Modeling subtype-selective agonists binding with α4β2 and α7 nicotinic acetylcholine receptors: Effects of local binding and long-range electrostatic interactions. *J. Med. Chem. 49*, 7661–7674.